



Complex frequency detection in a subsystem



Juntao Huang^{1,2}, Jiangping Hu^{3,4,5} & Zhesen Yang^{1,6}

Non-Hermitian physics, such as the non-Hermitian skin effect (NHSE), is well-established in classical platforms, but its emergence in intrinsically Hermitian or quantum systems remains a key challenge. Bridging this gap is crucial for connecting non-Hermitian concepts with foundational quantum many-body theory. Here, we systematically investigate this by studying a quantum subsystem with an effective non-Hermitian Hamiltonian arising from its exact frequency-dependent self-energy. We further employ complex-frequency detection, including excitation, synthesis, and fingerprint, to probe physical responses induced by complex driving frequencies. Our calculations reveal that both complex frequency excitation and synthesis are incompatible with the non-Hermitian approximation and cannot characterize the presence of the NHSE. In contrast, the complex-frequency fingerprint successfully detects the distinctive responses induced by the NHSE through the introduction of a double-frequency Green's function. Our work provides a platform for studying non-Hermitian physics and its unconventional response in quantum systems rigorously without relying on any approximations.

Non-Hermitian physics, particularly the non-Hermitian skin effect (NHSE), the phenomenon where an extensive number of non-orthogonal eigenstates become localized at the boundary^{1–7}, has recently attracted significant theoretical research interest^{5–13}. Many experimental developments have been made in classical wave platforms, including acoustic^{14–17}, optical^{18–22}, mechanical^{23–26}, and electrical circuit systems^{27–31}. These experiments have vividly demonstrated the existence of non-Hermitian skin modes in intrinsically dissipative systems. In many implementations, such as engineering asymmetric couplings in acoustic ring resonators¹⁵ and coupled optical fiber loops¹⁸, introducing gain and loss in photonic quantum walks¹⁹, the corresponding non-reciprocal or non-unitary dynamics associated with the NHSE have been further explored and corroborated.

However, these advances have predominantly involved phenomenological non-Hermitian terms, such as engineered gain and loss, implemented in classical wave platforms. In quantum systems, a key route to non-Hermitian descriptions originates from the self-energy within the Green's function formalism^{13,32–36}. In real-space representation, the retarded Green's function reads

$$G^R(\omega) = \frac{1}{\omega - H_0 - \Sigma(\omega)}, \quad (1)$$

where H_0 is the single-particle non-interacting Hamiltonian and $\Sigma(\omega)$ denotes the self-energy arising from, for example, electron-electron, electron-phonon, impurity, or substrate scattering. Since $\Sigma(\omega)$ is generally frequency-dependent, it is common practice to approximate it by a frequency-independent matrix, $\Sigma(\omega) \simeq \Sigma_0 = \Sigma(\omega = 0)$, i.e., an approach termed the non-Hermitian approximation (NHA):

$$G^R(\omega) \simeq G_{\text{nH}}^R(\omega) = \frac{1}{\omega - H_0 - \Sigma_0}. \quad (2)$$

This treatment often provides a good approximation to the spectral function and is widely employed in theoretical calculations. Under the NHA^{32,33,37–44}, the effective Hamiltonian

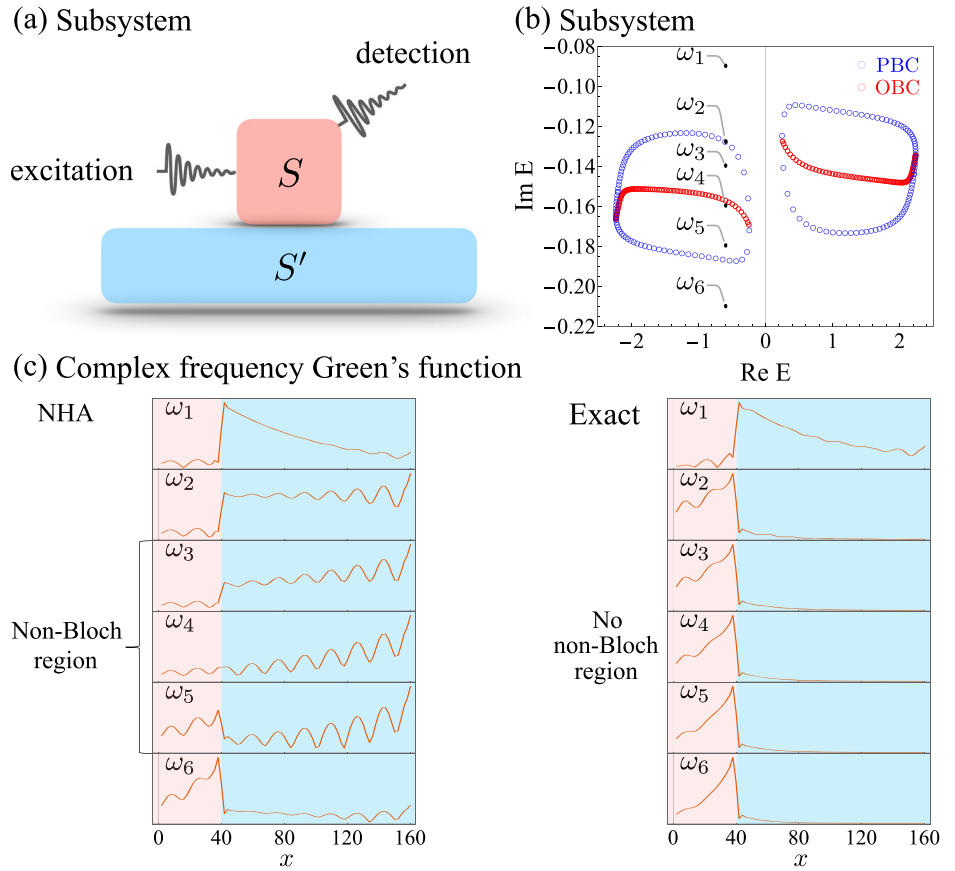
$$H_{\text{nH}} = H_0 + \Sigma_0 \quad (3)$$

becomes non-Hermitian and can exhibit point-gap topology along with the corresponding non-Hermitian skin effect.

Recently, complex frequency detection techniques, including complex frequency excitation (CFE)^{45–54}, synthesis (CFS)^{45,46,55}, and fingerprint (CFE)⁵⁶, have garnered significant attention. As the names suggest, these methods enable the experimental detection of the corresponding Green's

¹Department of Physics, Xiamen University, Fujian Province, Xiamen, China. ²Jiujiang Research Institute of Xiamen University, Jiujiang, China. ³Beijing National Laboratory for Condensed Matter Physics and Institute of Physics, Chinese Academy of Sciences, Beijing, China. ⁴School of Physical Sciences, University of Chinese Academy of Sciences, Beijing, China. ⁵New Cornerstone Science Laboratory, Beijing, China. ⁶Asia Pacific Center for Theoretical Physics, Gyeongbuk, Pohang, Republic of Korea. ✉e-mail: jphu@iphy.ac.cn; yangzs@xmu.edu.cn

Fig. 1 | Non-Bloch response in subsystem model.
a Schematic of subsystem S under excitation and detection, coupled to another subsystem S' .
b Spectra of $H_{S,nH}$ under periodic boundary condition (PBC) and open boundary condition (OBC), denoted by blue and red circles, respectively. The nontrivial spectral topology is obtained via Eq. (12). Here, $\omega_1 = -0.6 - 0.09i$, $\omega_2 = -0.6 - 0.128i$, $\omega_3 = -0.6 - 0.14i$, $\omega_4 = -0.6 - 0.16i$, $\omega_5 = -0.6 - 0.18i$ and $\omega_6 = -0.6 - 0.21i$.
c Comparative analysis of the complex frequency Green's function (red curve) obtained with and without the non-Hermitian approximation (NHA). The complex frequency Green's function (CFGF) is calculated via Eq. (11) and Eq. (8), respectively, under OBC. The pink and blue shading represents regions where $x \leq x_0$ and $x > x_0$ for $|G_S^R(\omega)|_{x,x_0}$ ($x_0 = 40$), respectively. Detailed model is illustrated in Fig. 2(a) and defined via Eq. (4)–Eq. (6). Parameters are $t_1 = 1.2$, $t_2 = -1$, $\lambda = -1$, $\mu_S = 0.2$, $t_x = 1$, $t_y = 3.5$, $\mu_S = 0.3$, $t_A = 0.6$, $\gamma = 0.1$, $N_S = 80$ and $N_y = 300$.



function in the complex frequency domain (see Supplementary Note 2). This naturally raises a fundamental question: Given that the non-Hermitian approximation works well on the real-frequency axis, how does its validity extend over the entire complex plane? Moreover, if we apply complex frequency detection to such systems, what physical outcomes would emerge?

To address this question, we propose a subsystem model as illustrated in Fig. 1(a). When both excitations and responses are confined within a subsystem S , a frequency-dependent self-energy emerges, i.e., $\Sigma_S(\omega)$. Compared to dealing with the interacting system, the self-energy in this subsystem approach is often more tractable, both analytically and numerically, making it a practical and well-motivated route to exploring the corresponding complex frequency detection.

Our conclusion can be summarized as follows: As illustrated in Fig. 1(b), in our subsystem model H_S , under the NHA, $H_{S,nH} = H_S + \Sigma_S(\omega = 0)$ exhibits non-zero spectral winding under the periodic boundary condition (PBC), and the corresponding non-Hermitian skin effect under open boundary condition (OBC)^{10,12}. Now we consider the complex frequency Green's function (CFGF) of $H_{S,nH}$ under OBC. As illustrated in Fig. 1(c), frequencies from ω_3 to ω_5 (which possess non-zero spectral winding) exhibit rightward-dominant divergence in the CFGF upon excitation at $x_0 = 40$. Such a divergent behavior is a hallmark of the non-Bloch response^{56–58} and can be used to characterize the presence of point gap topology as well as the NHSE^{10,12,59,60} (See Supplementary Note 1).

However, if we consider the exact frequency-dependent self-energy without any approximation, the corresponding complex frequency Green's function demonstrates that the unidirectional divergence becomes absent, as illustrated in Fig. 1(c) (right panel). This result raises three fundamental issues: (i) How to interpret this result? (ii) Does our subsystem truly exhibit the non-Hermitian skin effect and non-Bloch responses? (iii) What kind of result does the complex frequency detection method measure? Notably, as illustrated in Fig. 1(c), when ω lies near the real axis (e.g., ω_1), the exact and NHA Green's functions behave similarly. However, when ω lies near the PBC spectral regions, the differences between them become dominant.

Table 1 | Results of CFE, CFS, and CFF for $t \rightarrow \infty$

	Effective Region	CFGF	NHA	Non-Bloch Response
CFE	$\text{Im } \omega_c > -\gamma$	Eq. (8)	×	×
CFS	the same as CFE			
CFF	$\omega_r \in \mathbb{R}$	Eq. (26)	✓	✓

As summarized in Table 1, the long-time asymptotic behaviors of CFE and CFS yield the exact results with no non-Bloch response, whereas the CFF in the steady-state limit detects the approximated ones with the presence of non-Bloch response. Our work not only establishes a foundation for understanding the non-Hermitian skin effect and non-Bloch dynamics in quantum systems but also provides critical guidance for experimental verification.

Results and Discussion

Model and subsystem Green's function

Our Hamiltonian adopts the following Hermitian form:

$$\hat{H}_{\text{tot}} = \hat{H}_S + \hat{H}_{S'} + \hat{H}_{SS'}, \quad (4)$$

where the hopping parameters are illustrated in Fig. 2(a). The subsystem S corresponds to a one-dimensional spinless Rice-Mele model with broken time-reversal symmetry¹³, positioned in the $\gamma = 1$ region, with sublattices A and B represented by red and blue points, respectively. Applying the Fourier transformation, we obtain the Bloch Hamiltonian:

$$H_S(k) = (t_1 + t_2 \cos k)\sigma_x + t_2 \sin k \sigma_y + (\lambda \sin k - \mu_S)\sigma_z, \quad (5)$$

where the Pauli matrix acts on the sublattice degree of freedom. We denote the number of unit cells in S by N_S .

The subsystem S' comprises a two-dimensional single-band model inhabiting the $y \geq 2$ region, featuring anisotropic hoppings with $t_x \neq t_y$. Its x -direction Bloch Hamiltonian adopts the layer-resolved form:

$$H_{S'}(k) = \begin{pmatrix} h_{S'}(k) & t_y \sigma_0 & 0 & 0 & 0 & \dots \\ t_y \sigma_0 & h_{S'}(k) & t_y \sigma_0 & 0 & 0 & \dots \\ 0 & t_y \sigma_0 & h_{S'}(k) & t_y \sigma_0 & 0 & \dots \\ \dots & \dots & \dots & \dots & \dots & \dots \end{pmatrix}, \quad (6)$$

where $h_{S'}(k) = (t_x + t_x \cos k)\sigma_x + t_x \sin k\sigma_y - \mu_{S'}\sigma_0$ describes the Hamiltonian at each y -layer using a two-site unit cell. The interlayer hopping in the subsystem S' is parameterized by $t_y\sigma_0$, and the total number of y -layers in the subsystem S' is denoted as $N_{y'}$. Notably, although $\hat{H}_{S'}$ is intrinsically a single-band system along the x direction, we adopt a two-band representation for conceptual and notational convenience. This choice circumvents the band-folding issue that would otherwise arise in $\Sigma_S(k, \omega)$, thereby preserving momentum consistency between $H_S(k)$ and the self-energy. Importantly, the physical results, particularly the subsystem Green's function of S , remain unaffected by this representational choice, as they are determined solely by projecting the full Green's function onto the S subspace within the fixed total Hilbert space.

For conceptual clarity, we restrict inter-subsystem coupling to the A-sublattice (denoted as t_A ; qualitative results hold for any $t_B \neq t_A$, see Supplementary Note 8 and Fig. S3). In this case, as derived in Supplementary Note 3, the exact self-energy for the subsystem S becomes:

$$\Sigma_S(k, \omega) = \begin{pmatrix} \Sigma_S^{AA}(k, \omega) & 0 \\ 0 & 0 \end{pmatrix}, \quad (7)$$

where $\Sigma_S^{AA}(k, \omega) = t_A^2 [1/(\omega - H_{S'}(k))]_{11}$. Here, the subscript 11 denotes the (1, 1) matrix element of the Green's function for $H_{S'}(k)$ within its two-band representation, corresponding to the A-sublattice. Fig. 2(b, c) presents the corresponding density plots of the real and imaginary components of $\Sigma_S^{AA}(k, \omega)$, respectively. Based on this exact self-energy, the exact Green's function for subsystem S under PBC can be written as:

$$G_{S,\text{eff}}^R(k, \omega) = \frac{1}{\omega - H_{S,\text{eff}}(k, \omega)}, \quad (8)$$

where the frequency-dependent non-Hermitian Hamiltonian is explicitly expressed as

$$H_{S,\text{eff}}(k, \omega) = H_S(k) + \Sigma_S(k, \omega + i\gamma) - i\gamma. \quad (9)$$

Here, ω spans the entire complex energy plane, while the parameter $i\gamma$ serves as a trivial, constant dissipation, equivalent to the $i\eta$ in

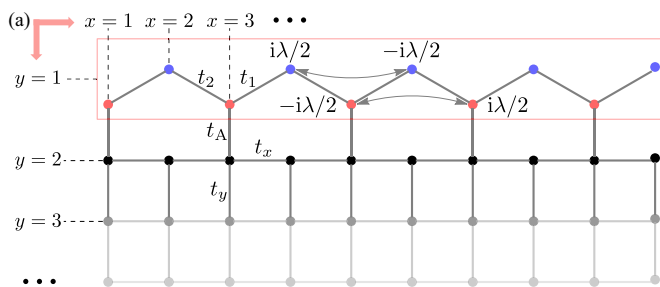


Fig. 2 | Model schematic and flat self-energy of the subsystem. **a** Schematic representation of the tight-binding model for the composite system, with subsystem S explicitly demarcated by the red rectangular enclosure. Here, red and blue dots correspond to atoms in sublattices A and B in S , respectively; the black dot represents the atom in S' ; black lines indicate chemical bonds; and a double-headed arrow marks the next-nearest hopping. **b** and **c** A comparison between the slowly varying

conventional retarded Green's function formalism of a Hermitian system. In practical numerical calculations, γ is chosen as a small value, which does not affect the qualitative results (See Supplementary Note 9 and Fig. S4–S6). Thus, the coupling to S' , or the self-energy, is necessary to induce nontrivial non-Hermitian physics, such as NHSE and non-Bloch phenomenon. It is precisely the detection of non-Bloch responses in a physically Hermitian system that demonstrates the significance of complex frequency detection, as discussed later. For notational simplicity, we retain the explicit $i\gamma$ in the self-energy but treat it as implicit in the frequency argument of $H_{S,\text{eff}}(k, \omega)$.

Non-Hermitian approximation

We now check the validity of the non-Hermitian approximation (NHA). As shown in Fig. 2(b) and (c), the two energy bands of $H_S(k)$, defined as $E_{\pm}(k)$, are plotted against the real and imaginary components of the self-energy, respectively. Notably, within the band dispersion region, the self-energy can be well approximated by a constant due to its negligible variation across the band (two orders of magnitude smaller than the bandwidth). Consequently, the expansion point $k = 0, \omega = 0$ (the band center of S) is chosen merely for convenience:

$$\Sigma_S^{AA}(k, \omega + i\gamma) \approx \Sigma_S^{AA}(0, i\gamma) + \mathcal{O}(k) + \mathcal{O}(\omega). \quad (10)$$

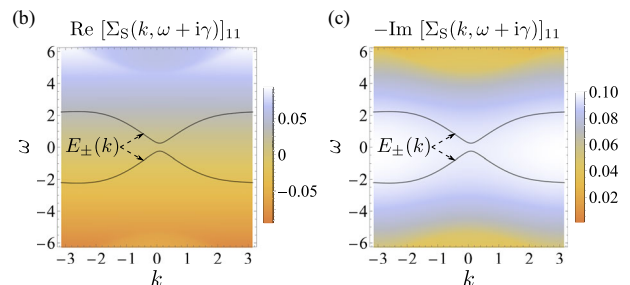
As further demonstrated in the Methods section, this negligible variation of the self-energy makes the choice of the approximation point arbitrary. This NHA yields the following approximated Green's function

$$G_{S,\text{nH}}^R(k, \omega) = \frac{1}{\omega - H_{S,\text{nH}}(k)}, \quad (11)$$

where the frequency-independent non-Hermitian Hamiltonian is given by:

$$H_{S,\text{nH}}(k) = H_S(k) + \begin{pmatrix} \Sigma_S^{AA}(0, i\gamma) & 0 \\ 0 & 0 \end{pmatrix} - i\gamma. \quad (12)$$

To further verify the non-Hermitian approximation, we present a comparative analysis of exact versus approximated spectral functions, i.e., $A_{S,\text{eff}/\text{nH}}(k, \omega) = -(1/\pi)\text{Im Tr } G_{S,\text{eff}/\text{nH}}^R(k, \omega \in \mathbb{R})$. As illustrated in Fig. 3(a) and (b), the precise agreement between these spectral functions confirms the validity of the NHA. This conclusion is further corroborated by the density of states (DOS) at real frequencies shown in Fig. 3(c), which follows the conventional definition, i.e., $\rho_{S,\text{eff}/\text{nH}}(\omega) = (1/N_S)\sum_k A_{S,\text{eff}/\text{nH}}(k, \omega)$. It should be noted, however, that this excellent agreement is confined to the real-frequency axis and deteriorates as the imaginary part of the frequency approaches the dissipation scale γ (see the validity domain analysis below).



self-energy and the bare bands $E_{\pm}(k)$ (marked by black lines) of the subsystem S . Here, the self-energy exhibits negligible variation (two orders of magnitude smaller than the bandwidth of S) across the band, which ensures the validity of the non-Hermitian approximation. The color bar in (b) and (c) ranges from -0.094 to 0.094 and 0.001 to 0.1 , respectively. The parameters include $t_1 = 1.2, t_2 = -1, \lambda = -1, \mu_S = 0.2, t_x = 1, t_y = 3.5, \mu_{S'} = 0.3, t_A = 0.6, \gamma = 0.1, N_S = 80$ and $N_{y'} = 300$.

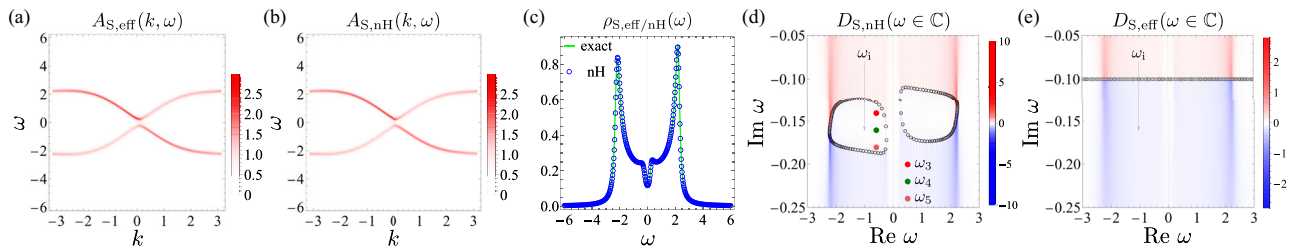


Fig. 3 | Verification of the non-Hermitian approximation at real and complex frequencies. The spectral functions under non-Hermitian approximation (NHA), $A_{S,nH}(k, \omega)$, and from the exact case, $A_{S,eff}(k, \omega)$, respectively. The color bar ranges are $[0.002, 2.98]$ for (a) and $[0.003, 2.99]$ for (b). c A comparison between the real frequency density of states (DOS) with and without the NHA, i.e., $\rho_{S,nH}(\omega)$ (blue circles) and $\rho_{S,eff}(\omega)$ (green curve), respectively. d, e The complex frequency DOS with and without NHA, defined as $D_{S,nH}(\omega \in \mathbb{C})$ and $D_{S,eff}(\omega \in \mathbb{C})$ respectively, where the black circles indicate the poles of the complex frequency Green’s function. The poles in (d) form the spectra with a nonzero winding number. The non-

Hermitian approximation remains accurate near the real axis but breaks down in the complex plane as $|\text{Im } \omega|$ increases. For (d) and (e), we choose $\omega = -1 - \omega_i$, with $\omega_i \in [0.08, 0.16]$ to compute the winding number shown in Fig. 8 in the “Methods” section. Frequencies from Fig. 1c’s non-Bloch region, i.e., $\omega_3, \omega_4, \omega_5 = -0.6 - 0.14i, -0.6 - 0.16i, -0.6 - 0.18i$ are marked in (d) as red, green, and pink dots, respectively. The color bar ranges are $[-10, 10]$ for (d) and $[-2.8, 2.8]$ for (e). Other parameters are $t_1 = 1.2, t_2 = -1, \lambda = -1, \mu_S = 0.2, t_x = 1, t_y = 3.5, \mu_S = 0.3, t_A = 0.6, \gamma = 0.1, N_S = 80$ and $N_y = 300$.

Importantly, as illustrated later in the “Methods” section and in Supplementary Note 4, the validity of NHA requires that the coupled environment S' possesses a sufficiently large number of degrees of freedom and a broad enough bandwidth compared to S . This explains our choice of a 2D anisotropic environment with $t_y > t_x$ (t_x sets the bandwidth scale for S) and a sufficiently large N_y .

However, significant discrepancies emerge when considering the complex frequency domain. Figure 1(c) demonstrates a representative example of these differences. For comprehensive analysis, we introduce the complex-frequency density of states⁵⁶ across the entire complex plane, i.e.,

$$D_{S,eff/nH}(\omega) = -\frac{1}{N_S \pi} \sum_k \text{Im Tr } G_{S,eff/nH}^R(k, \omega \in \mathbb{C}), \quad (13)$$

which serves not only as a tool for analytic continuation, revealing the pole structures of the complex frequency Green’s function⁵⁶, but also as an indirect observable that faithfully captures the system’s underlying quasi-particle picture in the complex plane. As shown in Figs. 3(d, e), the approximated CFGF displays two closed-loop poles, contrasting with the exact case that features a branch cut positioned at $\text{Im } \omega = -\gamma$ (See Supplementary Note 5 for demonstration). Due to the vanishing of the spectral winding in the exact poles under PBC, it is expected that there is no non-Bloch response in the complex frequency Green’s function, which explains the paradox observed in Fig. 1(c). However, despite their distinct distributions, a profound connection exists: both the NHA loop-poles and the exact branch cut poles can be linked through an electrostatic mapping, as they generate an identical “electric field” along the real frequency axis. See Supplementary Note 7 for details.

As an aside, the poles of the Matsubara Green’s function are related to those of the complex frequency Green’s function by a Wick rotation and a constant γ -shift, detailed in Supplementary Note 6.

In summary, although the non-Hermitian approximation demonstrates excellent performance in simulating real-frequency Green’s function, it fundamentally modifies the global pole structures. The very success of the NHA in simulating real-frequency observables masks the fundamental disparity in the complex plane, thereby highlighting the critical need for our advanced approach to uncover genuine non-Bloch physics. Therefore, it is necessary to examine the nontrivial roles of the non-Hermitian approximation in variant complex-frequency detection methodologies.

Driven-dissipative equation

We now focus on the complex frequency detection of the subsystem. The theoretical framework originates from the following driving dissipative

equation⁵⁶:

$$i \frac{d\langle \hat{\mathbf{a}}(t) \rangle}{dt} = (H_{\text{tot}} - i\gamma)\langle \hat{\mathbf{a}}(t) \rangle + \mathbf{F}(t), \quad (14)$$

where H_{tot} represents the first quantized Hamiltonian of \hat{H}_{tot} in real space. The parameter γ characterizes the uniform dissipation within the Green’s function. As detailed in Supplementary Note 2, $\langle \hat{\mathbf{a}}(t) \rangle = \text{Tr} [\hat{\mathbf{a}}\hat{\rho}(t)] = \{ \langle \hat{\mathbf{a}}_S(t) \rangle, \langle \hat{\mathbf{a}}_C(t) \rangle \}^T$ describes the mean values of single-particle bosonic operators at each lattice site of the total system within the open quantum system framework. Here, $\hat{\mathbf{a}} = (\hat{a}_1, \hat{a}_2, \dots, \hat{a}_N)^T$ denotes the bosonic annihilation operator over the total system, N is the matrix dimension of H_{tot} , and $\hat{\rho}(t)$ is the density matrix operator. $\mathbf{F}(t)$ denotes the external drive. Experimentally, when $\mathbf{F}(t)$ is applied to the subsystem S , the corresponding response $\langle \hat{\mathbf{a}}_S(t) \rangle$ is detected. For example, consider an external driving defined as

$$\mathbf{F}(t) = \theta(t)e^{-i\omega_r t} \{0, \dots, 0, F_{S,j}, 0, \dots, 0\}^T, \quad \omega_r \in \mathbb{R}, \quad (15)$$

which acts exclusively on the i th-site of the subsystem S . Following Supplementary Note 2, the induced response at the j -th site, i.e., $\langle \hat{\mathbf{a}}_{S,j}(t) \rangle$, which is the direct experimental observable, demonstrates proportionality to the real-frequency Green’s function in the long-time limit. This relationship can be expressed as:

$$\lim_{t \rightarrow \infty} \langle \hat{\mathbf{a}}_{S,j}(t) \rangle = \left[G_{S,eff}^R(\omega_r) \right]_{ji} F_{S,i} e^{-i\omega_r t}, \quad (16)$$

where $G_{S,eff}^R(\omega_r)$ denotes the exact Green’s function of the subsystem defined in Eq. (8) (real space representation), and ω_r corresponds to the driving frequency. Given the predetermined values of $F_{S,i}$ and ω_r , the real-frequency Green’s function becomes experimentally accessible through $\langle \hat{\mathbf{a}}_{S,j}(t) \rangle$ detection. This methodology maintains alignment with classical wave system protocols for real-frequency Green’s function measurement^{61–65}.

Complex frequency excitation

When extending the driving frequency from real (ω_r) to complex values (ω_c) in Eq. (15), the concept of complex frequency excitation (CFE) emerges. As demonstrated in Supplementary Note 2, the experimental procedure of the CFE is largely identical to that of the CFF, except that the harmonic driving field is replaced by one with temporal attenuation. Specifically, the solution

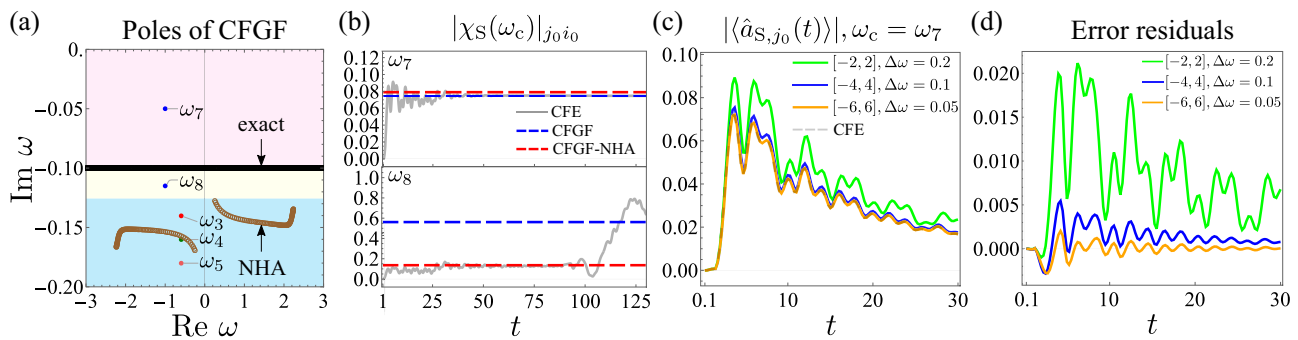


Fig. 4 | Comparison of complex frequency excitation and synthesis. **a** The poles of the subsystem complex frequency Green’s function with and without non-Hermitian approximation under (NHA) open boundary conditions (OBC). In the complex plane, the light pink shading represents the region within the branch cut, and the blue shading represents the area beyond the non-Hermitian spectra. The area between them is shaded light yellow. **b** A comparison between the time-dependent response function $\chi_S(\omega_c)$ for the complex frequency excitation (CFE, gray curve), and the complex frequency Green’s function with (red dashed line) and without NHA (blue dashed line). The result is obtained under OBC, exhibiting the failure of NHA in the complex plane. Here $\omega_7 = -1 - 0.05i$, $\omega_8 = -1 - 0.115i$, and $\omega_3 \sim \omega_5$ in Fig. 1c are marked as red, green, and pink dots, respectively. $j_0 = 30$, and

$i_0 = 36$. **c** A comparison of the observable $\langle \hat{a}_{S,j_0}(t) \rangle$ between the CFE (gray curve) and complex frequency synthesis (CFS) at ω_7 with different synthesis domains and spectral resolution (green, blue, and orange curves, respectively). Here $i_0 = 36$. Crucially, the line $\text{Im } \omega = -\gamma$ serves as a critical boundary: CFE (and equivalently CFS) responses undergo a qualitative change from steady-state convergence to divergence when crossing it. **d** Error analysis of the CFS. The error residuals, defined as the relative difference of the complex frequency synthesis (CFS) results from the complex frequency excitation (CFE) results in (c) (green, blue and orange curves, respectively). Other parameters are $t_1 = 1.2, t_2 = -1, \lambda = -1, \mu_S = 0.2, t_x = 1, t_y = 3.5, \mu_S' = 0.3, t_A = 0.6, \gamma = 0.1, N_S = 80$ and $N_Y = 300$.

to Eq. (14) under complex frequency driving

$$\mathbf{F}(t) = \theta(t)e^{-i\omega_c t} \{0, \dots, 0, F_{S,i}, 0, \dots, 0\}^T, \quad \omega_c \in \mathbb{C}, \quad (17)$$

takes the form

$$\langle \hat{a}_{S,j}(t) \rangle = [\chi_S(\omega_c)]_{ji} F_{S,i} e^{-i\omega_c t}, \quad (18)$$

where the response function $\chi_S(\omega_c)$, serving as the key CFE observable, is expressed as

$$\chi_S(\omega_c) = G_{S,\text{eff}}^R(\omega_c) - [G_{\text{tot}}^R(\omega_c) e^{-i(H_{\text{tot}} - i\gamma - \omega_c)t}]_S. \quad (19)$$

denotes the complex frequency Green’s function for the total system. We note that this solution assumes the initial condition $\langle \hat{\mathbf{a}}(0) \rangle = 0$, whose value will not affect the subsequent conclusions, as proved in Supplementary Note 2.

A critical observation arises from the above formulation: when the complex frequency ω_c resides above the branch cut determined by $i\gamma$ (light pink region in Fig. 4(a)), the corresponding response function will converge to the exact CFGF of the subsystem in the $t \rightarrow \infty$ limit, i.e.,

$$\lim_{t \rightarrow \infty} \chi_S(\omega_c) = G_{S,\text{eff}}^R(\omega_c), \quad \text{Im } \omega_c > -\gamma. \quad (20)$$

Conversely, frequencies below the $i\gamma$ line will yield divergent responses due to the second term’s divergence. A compact demonstration can be made by expanding the response function as

$$\chi_S(\omega_c) = P \sum_{n=1}^N \frac{|\psi_n\rangle \langle \psi_n|}{\omega_c + i\gamma - \epsilon_n} (\mathbf{I} - e^{-i(\epsilon_n - i\gamma - \omega_c)t}) P^\dagger, \quad (21)$$

where $P = (I_{2N_S \times 2N_S}, 0_{2N_S \times (N-2N_S)})$ denotes the projection matrix, and $|\psi_n\rangle$ and ϵ_n denote the eigenstates and eigenvalues of the Hermitian matrix H_{tot} under OBC. Notably, by Taylor expansion of the exponential function, one can see that Eq. (21) has no poles; thus, $\text{Im } \omega_c = -\gamma$ becomes the convergence boundary. As numerically verified in Fig. 4(b), only the ω_7 case converges to the exact CFGF (blue dashed lines).

For comparative analysis, we show the NHA-predicted complex frequency Green’s function as red dashed lines, which exhibit clear deviations

from our calculated response functions. This discrepancy stems from the modification of CFGF pole structures under the non-Hermitian approximation (Fig. 3(d, e)), rendering it invalid for frequencies distant from the real axis. The failure originates near the system’s exact poles, where the approximation error becomes singular, rendering the perturbative expansion invalid. Fig. 4(b) explicitly demonstrates this limitation: for ω_7 , converged results deviate from NHA predictions; ω_8 exhibits response divergence despite NHA suggesting convergence.

Key conclusions are summarized in Table 1: (i) The CFE exclusively detects the exact complex frequency Green’s function, i.e., Eq. (8), above the total Hamiltonian’s imaginary gap (light pink region); (ii) NHA fails in regions far from the real axis, an incompatibility that holds in the case of a frequency-dependent self-energy; (iii) Absence of non-Bloch response in long-time dynamics due to the vanishing of the spectral winding number.

Complex frequency synthesis

We now examine the complex frequency synthesis (CFS), a method based on the following observation: within the framework of CFE, the nonzero component of $\mathbf{F}(t)$ in Eq. (17) can be transformed through Fourier analysis as

$$\theta(t)e^{-i\omega_c t} = \frac{1}{2\pi} \int_{-\infty}^{\infty} \frac{i}{\omega - \omega_c} e^{-i\omega t} d\omega, \quad (22)$$

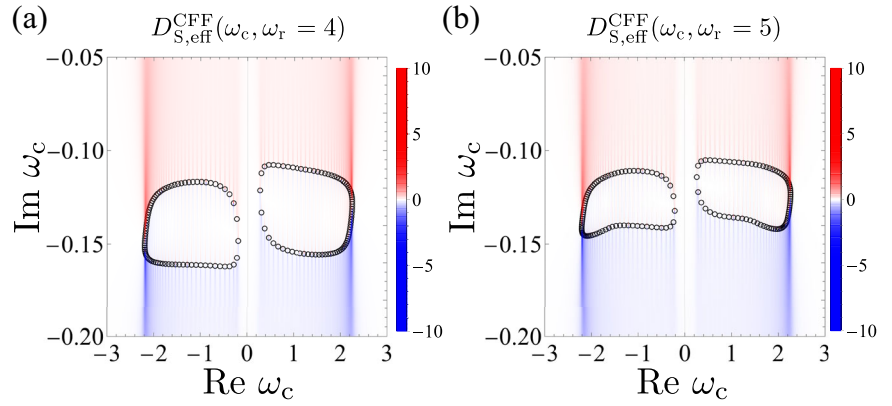
where $\text{Im } \omega_c < 0$ and $t > 0$. Experimentally measured real frequency responses enable comprehensive reconstruction of the CFE solution through signal synthesis (see Supplementary Note 2):

$$\langle \hat{\mathbf{a}}_{S,\omega_c}(t) \rangle = \frac{i}{2\pi} \sum_{\omega=\omega_a}^{\omega_b} \frac{\Delta\omega}{\omega - \omega_c} \langle \hat{\mathbf{a}}_{S,\omega}(t) \rangle, \quad (23)$$

where $[\omega_a, \omega_b]$ defines the synthesis domain and $\Delta\omega$ specifies the spectral resolution defined as the sampling interval between adjacent discrete frequencies. Following the measurement steps detailed in supplementary Note 2, the key observables of the CFS are the series of $\langle \hat{\mathbf{a}}_{S,\omega}(t) \rangle$ within the synthesis domain. The quantity $\langle \hat{\mathbf{a}}_{S,\omega_c}(t) \rangle$ is the numerically synthesized result.

As summarized in Table 1, CFS demonstrates theoretical equivalence with CFE. Specifically, as detailed in Supplementary Note 2, the established

Fig. 5 | The results of complex frequency fingerprint. a, b The complex frequency density of states for the complex frequency fingerprint (CFF) defined as $D_{S,\text{eff}}^{\text{CFF}}(\omega_c, \omega_r)$ at $\omega_r = 4$ and $\omega_r = 5$, respectively. Both results in (a) and (b) exhibit nontrivial spectral topology, with the color bar ranging from -10 to 10 . The poles of the double-frequency Green's function are marked by black circles. Other parameters are $t_1 = 1.2, t_2 = -1, \lambda = -1, \mu_S = 0.2, t_x = 1, t_y = 3.5, \mu_{S'} = 0.3, t_A = 0.6, \gamma = 0.1, N_S = 80$ and $N_y = 300$.



exact identity:

$$\langle \hat{\mathbf{a}}_{S,\omega_c}(t) \rangle = \frac{i}{2\pi} \int_{-\infty}^{\infty} \frac{1}{\omega - \omega_c} \langle \hat{\mathbf{a}}_{S,\omega}(t) \rangle d\omega \quad (24)$$

serves as rigorous proof of this equivalence. A quantitative validation is presented in Fig. 4(c), where the result derived from CFE is compared with synthesized responses across progressively expanding synthesis domains and refined spectral resolutions $\Delta\omega$. The convergence toward the CFE result confirms the validity of the CFS method, which is further verified by the error residuals in Fig. 4(d).

Complex frequency fingerprint

To capture the non-Bloch response, the recently developed complex frequency fingerprint (CFF) method under real-frequency driving is necessary. Its experimental implementation comprises three concise steps (details in Supplementary Note 2 and Fig. S1): (i) Apply a harmonic drive $F_i(t) = \theta(t)e^{-i\omega_r t} F_{S,i}$ at a single site i and measure the induced response $\langle \hat{a}_j(t) \rangle_{F_i}$ at all sites j within subsystem S ; (ii) repeat step (i) sequentially for every site $i = 1, \dots, 2N_S$ to construct the full response matrix $\chi_S(\omega_r, t)$, with elements $[\chi_S(\omega_r, t)]_{ji} = \langle \hat{a}_j(t) \rangle_{F_i} / (F_{S,i} e^{-i\omega_r t})$; (iii) define the CFF as

$$\mathcal{G}_{S,\omega_r}(\omega_c \in \mathbb{C}; t) = \frac{1}{(\omega_c - \omega_r) + [\chi_S(\omega_r, t)]^{-1}}, \quad (25)$$

with an auxiliary parameter ω_c . As demonstrated in Supplementary Note 2, as $t \rightarrow \infty$, the CFF specifically measures the following double-frequency Green's function,

$$G_{S,\text{eff}}^{\text{CFF}}(k, \omega_c, \omega_r) = \frac{1}{\omega_c - H_{S,\text{eff}}(k, \omega_r)}, \quad (26)$$

where $\omega_c \in \mathbb{C}$ and $\omega_r \in \mathbb{R}$. Notably, here we clarify that as detailed in Supplementary Note 2, ω_c and ω_r in the CFF method are independent parameters: ω_c is an artificially introduced complex variable, while ω_r is a controlled parameter corresponding to the frequency of the actual driving field defined in Eq. (15). Crucially, for any fixed driving parameter ω_r , this double-frequency Green's function precisely corresponds to the CFGF associated with the non-Hermitian Hamiltonian $H_{S,\text{eff}}(k, \omega_r)$. As ω_r evolves, the corresponding double-frequency Green's function changes accordingly. Figure 5(a) and (b) exemplify this behavior through the following complex-frequency DOS

$$D_{S,\text{eff}}^{\text{CFF}}(\omega_c, \omega_r) = -\frac{1}{N_S \pi} \sum_k \text{Im Tr } G_{S,\text{eff}}^{\text{CFF}}(k, \omega_c, \omega_r) \quad (27)$$

at frequencies $\omega_r = 4$ and $\omega_r = 5$, respectively.

For any given ω_r , once $H_{S,\text{eff}}(k, \omega_r)$ exhibits the NHSE, the corresponding non-Bloch response can be detected via the double-frequency Green's function by setting ω_c with a nonzero spectral winding. An example is illustrated on the left side of Fig. 1(c) with $\omega_r = 0$. Moreover, for the non-Hermitian skin effect in $H_{S,\text{eff}}(k, \omega_r)$ to be pronounced, ω_r must lie within the spectral range of S' . If ω_r lies far outside this region, the self-energy becomes vanishingly small, causing the NHSE, even if theoretically present, to be imperceptible. Furthermore, the nonzero spectral winding originates primarily from two intrinsic properties of subsystem S : the breaking of time-reversal symmetry and its asymmetric coupling to S' ($t_A \neq t_B$)¹⁵. It is not explicitly tied to the topological properties of the full system \hat{H}_{tot} .

In summary, as illustrated in Table 1: (i) The CFF methodology effectively identifies double-frequency Green's function governed by Eq. (26); (ii) For each driving frequency ω_r , the CFF is described by the non-Hermitian Hamiltonian at ω_r , i.e., $H_{S,\text{eff}}(k, \omega_r)$; (iii) This framework establishes a unified platform for the systematic exploration of NHSE and non-Bloch responses in a Hermitian quantum system.

Notably, the inequivalence between CFF and CFE primarily stems from the frequency dependence of the self-energy, reflecting the breakdown of the Markovian approximation. However, even when the Markovian approximation is valid, if the subsystem Hamiltonian \hat{H}_S is intrinsically non-Hermitian and hosts nontrivial spectral topology, CFE and CFF remain inequivalent due to virtual gain (divergent response from CFE, see Supplementary Note 2). Meanwhile, the CFF approach continues to correctly capture the response across the full complex-frequency plane under real-frequency excitation⁵⁶.

Conclusion

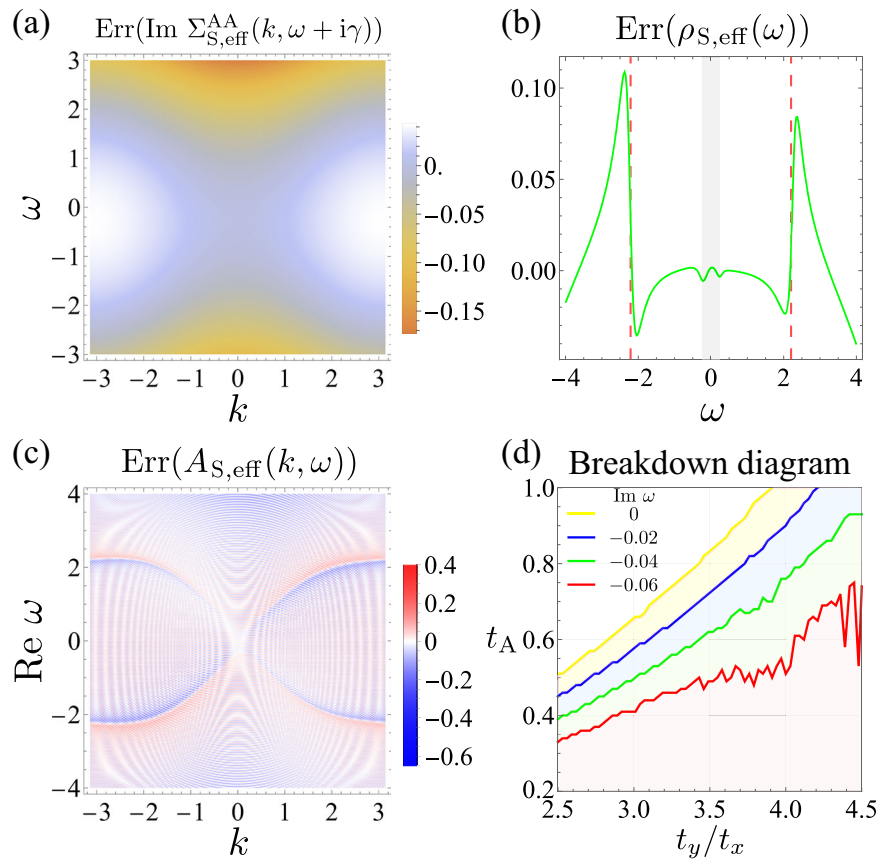
In this work, we have established a framework for detecting complex frequency responses in a frequency-dependent Hamiltonian of the subsystem. Our comparative study reveals that while both CFE and CFS methods yield identical results characterizing the exact complex frequency Green's function without non-Hermitian skin effect signatures, the CFF approach uniquely manifests non-Bloch responses through its detection of double-frequency Green's function. Our work elucidates the physical origin of non-Hermitian Hamiltonians in quantum systems through exact theoretical formalisms, bypassing traditional approximation constraints. These advancements provide foundational insights for decoding non-Hermitian phenomena in quantum systems and offer concrete guidance for experimental implementations.

Methods

Validity domain analysis of the NHA

We perform an error analysis to determine the validity domain of the self-energy under the non-Hermitian approximation. For this purpose, we define a relative error function, e.g., $\text{Err}(\text{Im } \Sigma_{S,\text{eff}}^{\text{AA}}(k, \omega + i\gamma)) = 1 - \text{Im } \Sigma_{S,\text{eff}}^{\text{AA}}(0, 0 + i\gamma) / \text{Im } \Sigma_{S,\text{eff}}^{\text{AA}}(k, \omega + i\gamma)$, $\text{Err}(\rho_{S,\text{eff}}(\omega)) = 1 - \rho_{S,\text{NH}}(\omega) / \rho_{S,\text{eff}}(\omega)$ and $\text{Err}(A_{S,\text{eff}}(k, \omega)) = 1 - A_{S,\text{NH}}(k, \omega) / A_{S,\text{eff}}(k, \omega)$, which quantifies

Fig. 6 | Error analysis of the NHA: deviation from the exact result. a Relative error of the imaginary part of the self-energy. The color bar ranges from -0.17 to 0.04 . **b** Relative error of the density of states (DOS, green curve); the red dashed lines mark band edges at $\omega = \pm 2.21$, and the gray shaded areas indicate the band gaps (≈ 0.5). **c** Relative error of the spectral function at $\text{Im } \omega = -0.08$. The color bar ranges from -0.65 to 0.4 . **d** Validity breakdown diagram of the non-Hermitian approximation (NHA) versus $\text{Im } \omega$, t_A and t_y/t_x . Boundary lines are drawn as yellow, blue, green, and red curves, with their corresponding validity regions filled with the respective colors. Here, $t_1 = 1.2$, $t_2 = -1$, $\lambda = -1$, $\mu_S = 0.2$, $t_x = 1$, $\mu_{S'} = 0.3$, $\gamma = 0.1$, $N_S = 80$ and $N_y = 300$, $E_{\min} = -2.21$, $E_{\max} = 2.21$. In (a)–(c) $t_y = 3.5$, $t_A = 0.6$.



the deviation of the NHA result from the exact counterpart. Notably, here the subscript “eff” emphasizes the case of exact frequency-dependent effective Hamiltonian in Eq. (8). As shown in Fig. 6(a), the relative error in the imaginary part of the self-energy remains negligible (below 5%) within the subsystem bandwidth, demonstrating the validity of the NHA in this region, as well as the free choice of the approximation point beyond $k = 0, \omega = 0$. Moreover, as previously indicated in Fig. 2(b), the real part of the self-energy varies only slightly over the same bandwidth, further supporting the accuracy of the approximation. This validity domain is also corroborated by Fig. 6(b), where the relative error of the DOS stays sufficiently small between the band edges (marked by red dashed lines).

Outside the bandwidth, the relative error of the imaginary part of the self-energy grows significantly, exceeding 10%, indicating the breakdown of the non-Hermitian approximation. Nevertheless, since the density of states decays rapidly in this region, the NHA remains applicable on the real frequency axis.

In contrast, the non-Hermitian approximation fails in the complex plane. As illustrated in Fig. 6(c), the spectral function at $\text{Im } \omega = -0.08$ exhibits substantial errors under the NHA, even within the bandwidth, highlighting the limitation of the method for complex frequencies.

To illustrate the validity domain of non-Hermitian approximation with respect to $\text{Im } \omega$, t_A and t_y/t_x , we again employ the error function for the density of states, $\text{Err}(\rho_{S,\text{eff}}(\omega))$. The condition $\text{Im } \omega > -\gamma$ ensures that the DOS $\rho_{S,\text{eff/nH}}(\omega)$ is well-defined along $\text{Re } \omega$. Specifically, we scan the relative error across $\text{Re } \omega \in [E_{\min}, E_{\max}]$, where E_{\min}/max denote the lower/upper band edge of $H_S(k)$. The NHA is considered to fail whenever the relative error exceeds 5% at any $\text{Re } \omega$ within this interval. As shown in Fig. 6(d), the shaded regions below the curves, each corresponding to a different $\text{Im } \omega$, indicate where the non-Hermitian approximation remains valid. Above these curves, the approximation fails, indicating the necessity of an anisotropic environment S' with a bandwidth sufficiently broad relative to S . Notably, as $\text{Im } \omega$ approaches the branch cut, the validity region shrinks and

the boundaries become more unstable (oscillatory), suggesting that a larger N_y is required to converge the self-energy at higher t_y/t_x ratios.

Furthermore, we consider the separability of ω_c and ω_r in the double-frequency density of states $D_{S,\text{eff}}^{\text{CF}}(\omega_c, \omega_r)$, which relates to the validity of the non-Hermitian approximation. The essential information for the complex-frequency DOS is contained in the eigenvalues of the effective non-Hermitian Hamiltonian $H_{S,\text{eff}}(k, \omega_r)$. The distribution of its eigenvalues thus serves to characterize the validity of the NHA.

Specifically, under the NHA at $\omega_r = 0$, the eigenvalue trajectories form loops enclosing a fixed area. As ω_r varies, the point gap topology persists, but the shape and area of these loops change. Thus, we can define $\text{Ar}_{\text{eff}}(\omega_r)$ as the area enclosed by the eigenvalue loops of $H_{S,\text{eff}}(k, \omega_r)$. Then the validity of the non-Hermitian approximation can be quantified by the relative error function $\text{Err}(\text{Ar}_{\text{eff}}(\omega_r)) = 1 - \text{Ar}_{\text{eff}}(0)/\text{Ar}_{\text{eff}}(\omega_r)$. As shown in Fig. 7, using a 5% relative error as the demarcation standard, the validity domain of the NHA is indicated by the light blue shaded area, where the relative error remains within 5%, exhibiting the separability of ω_c and ω_r within this region. Beyond this threshold, in the light pink shaded region, the non-Hermitian approximation begins to fail, and the exact treatment should be considered. This result clearly demonstrates the dependence of the complex DOS on ω_r , underscoring its inherent double-frequency nature.

The loop-cut tracking method and the winding number

Here, we provide a quantitative diagnostic tool for verifying the point gap topology and the branch cut beyond mere visual plotting.

For the NHA case, we consider $E_1(k)$ and $E_2(k)$ as the two sets of eigenvalues of $H_{S,\text{nH}}(k)$. As shown in Fig. 3(d), these eigenvalues form the two distinct loops on the complex plane. In our numerical calculation, we discretize the momentum as $k_i = -\pi + (i - 1)\frac{2\pi}{N_S}$ with $i = 1, 2, \dots, N_S$. Focusing on $E_1(k)$ as an example (the left loop in Fig. 3(d)), we define the relative phase angle between consecutive eigenvalues as $\theta(k_i) = \text{Arg}(E_1(k_{i+1}) - E_1(k_i))$, where Arg returns the phase within $[-\pi, \pi]$.

As shown in Fig. 8(a), the blue circles indicate the evolution of this relative phase for $N_S = 80$. The complete 2π transition clearly tracks the winding of $E_1(k)$ and demonstrates the existence of a loop. The result is further confirmed by the results for $N_S = 300$ (marked by crosses), which show convergence. This outcome can be verified by the winding number defined in Supplementary Note 1:

$$\nu_{\text{nH}}(\omega) = \frac{1}{2\pi i} \int_{-\pi}^{\pi} dk \partial_k \ln \det[H_{\text{nH}}(k) - \omega]. \quad (28)$$

In this case, we choose $\omega = -1 - \omega_i i$ with $\omega_i \in [0.08, 0.16]$. As ω_i varies, this frequency trajectory crosses the loop in Fig. 3(d) and the branch cut in Fig. 3(e). As shown in Fig. 8(c), the corresponding winding number jumps

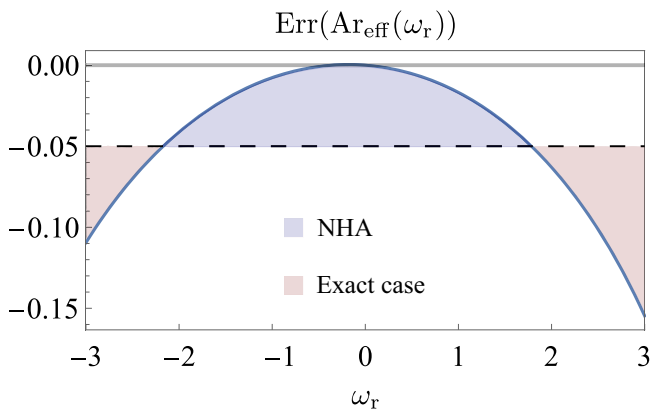


Fig. 7 | Evolution of the ω_r -dependence from negligible to significant. The relative error in the area enclosed by the eigenvalues of $H_{S,\text{eff}}(k, \omega_r)$ as a function of ω_r , using a 5% threshold (the black dashed line) to indicate the validity of non-Hermitian approximation (light blue and light pink regions represent validity and failure, respectively). Here, $t_1 = 1.2, t_2 = -1, \lambda = -1, \mu_S = 0.2, t_x = 1, t_y = 3.5, \mu_{S'} = 0.3, t_A = 0.6, \gamma = 0.1, N_S = 80$ and $N_y = 300$.

from zero to one when the complex frequency encounters the loop, demonstrating the point gap topology.

For the exact case, it can be proved (see Supplementary Note 5) that the poles are given by the eigenvalues of

$$H_{\text{tot}}(k) - i\gamma = \begin{pmatrix} H_S(k) & H_{SS'} \\ H_{SS'}^\dagger & H_{S'}(k) \end{pmatrix} - i\gamma \quad (29)$$

is

$$H_{SS'} = \begin{pmatrix} t_A & 0 & 0 & \dots & 0 \\ 0 & t_B & 0 & \dots & 0 \end{pmatrix}, \quad (30)$$

which is a $2 \times 2N_y$ matrix. Similarly, we denote the eigenvalues of $H_{\text{tot}}(k) - i\gamma$ as $\epsilon_1(k), \epsilon_2(k), \dots, \epsilon_{2N_y+2}(k)$, and analyze $\epsilon_1(k)$ to examine its “cut” property. The result in Fig. 8(b) shows numerically negligible variation ($\sim 10^{-7}$, which originates from the inherent truncation error of the numerical diagonalization process), indicating that these poles share the same imaginary part, thus forming a cut. This conclusion is further confirmed by the winding number

$$\nu_{\text{ext}}(\omega) = \int_{-\pi}^{\pi} dk \partial_k \ln \det[H_{\text{tot}}(k) - \omega - i\gamma]. \quad (31)$$

As shown in Fig. 8(d), the vanishing winding number demonstrates the trivial spectral topology of the branch cut.

Quantitative verification of the non-Bloch region

This section provides a quantitative demonstration of the non-Bloch region in Fig. 1, going beyond the visual representation. For clarity, we define the spatial distribution of the Green’s function under NHA as

$$\psi_{\text{nH},i}(\omega) = \sqrt{|[G_{S,\text{nH}}^R(\omega)]_{2i-1,j_0}|^2 + |[G_{S,\text{nH}}^R(\omega)]_{2i,j_0}|^2}_{\text{Nor}}, \quad (32)$$

Fig. 8 | Diagnostic verification of the loop and the branch cut. **a, b** The tracked relative phase of eigenvalues (poles) for the non-Hermitian approximation (NHA) and the exact case, respectively. Blue circles and brown crosses represent the case of $N_S = 80$ and $N_S = 300$, respectively. **c, d** The corresponding winding number (red circles) for the NHA and exact case, with $\omega = -1 - \omega_i i$, where $\omega_i \in [0.08, 0.16]$. These results confirm the presence of loop and branch cut characteristics.

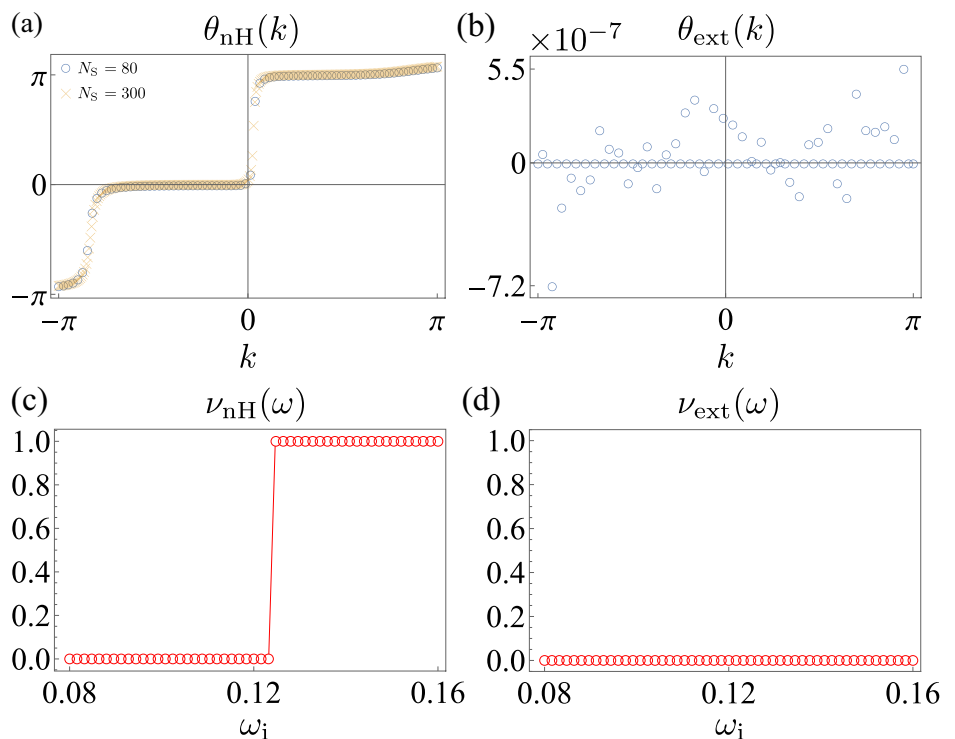
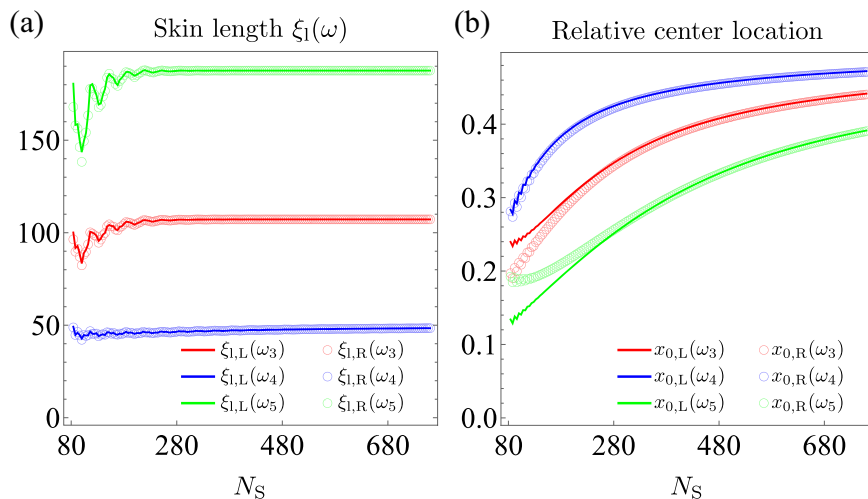


Fig. 9 | Quantitative evidence of the non-Bloch response. **a** The skin length $\xi_{i,L}(\omega)$ (lines) and $\xi_{i,R}(\omega)$ (circles) for ω_3, ω_4 and ω_5 (red, blue and green colors, respectively) in the non-Bloch region of Fig. 1(c), which converges as N_S increases. Excitation sites are $j_0 = 40$ ($\lambda = -1$) and $j_0 = 2N_S - 39$ ($\lambda = 1$). **b** The relative center location $x_{0,L}$ (lines) and $x_{0,R}$ (circles) of $\psi_{nH}(\omega)$ approaches 0.5 for ω_3, ω_4 and ω_5 (red, blue and green colors, respectively) as N_S increases, which demonstrates the non-reciprocal localization. Here $\omega_3, \omega_4, \omega_5 = -0.6 - 0.14i, -0.6 - 0.16i, -0.6 - 0.18i$. All other parameters are $t_1 = 1.2, t_2 = -1, \mu_S = 0.2, t_x = 1, t_y = 3.5, \mu_S' = 0.3, t_A = 0.6, \gamma = 0.1$ and $N_y = 300$.



where $i = 1, 2, \dots, N_S$ and $|\cdot|_{\text{Nor}}$ denotes normalization. To characterize the skin effect, we introduce the skin length $|\xi_i(\omega)|$ through the relation $\ln \psi_{nH,i}(\omega) \sim i/\xi_i(\omega)$, with ω belonging to the non-Bloch region. Since the exponential scaling requires using bulk sites away from boundaries to avoid edge effects, we numerically fit $\ln \psi_{nH}(\omega)$ over the sites $i \in [N_S/4, 3N_S/4]$. This choice is arbitrary but does not affect the steady-state results as $N_S \rightarrow \infty$.

For ω in the non-Bloch region and $\lambda < 0$ (the sign of λ does not affect the complex spectrum), we find $\xi_i(\omega) > 0$. With a left-side excitation at $j_0 = 40$, $\psi_{nH}(\omega)$ localizes to the right, so we denote $\xi_{i,L}(\omega) = \xi_i(\omega)$ for $\lambda < 0$. Conversely, for $\lambda > 0$ and a right-side excitation at $j_0 = 2N_S - 39$, $\psi_{nH}(\omega)$ localizes to the left, and we define $\xi_{i,R}(\omega) = -\xi_i(\omega)$ for $\lambda > 0$.

Figure 9(a) shows that the skin length converges to definite values as N_S increases. The coincidence of $\xi_{i,L}$ and $\xi_{i,R}$ at large N_S demonstrates left/right excitation symmetry. The steady-state skin lengths for $\omega_3, \omega_4, \omega_5$ are obtained as 107.2, 48.4, and 187.7, respectively.

Next, to quantify left-right asymmetry in the non-Bloch region, we define the distribution center:

$$x_0(\omega) = \frac{1}{N_S} \sum_{i=1}^{N_S} i |\psi_{nH,i}(\omega)|^2, \quad (33)$$

where $x_0(\omega) \in (0, 1)$. Values $x_0(\omega) > 0.5$ ($\lambda < 0$) indicate rightward localization, while $x_0(\omega) < 0.5$ ($\lambda > 0$) indicate leftward localization. For convenience, we define the relative center location as $x_{0,L}(\omega) = x_0(\omega) - 0.5$ ($\lambda < 0$) and $x_{0,R}(\omega) = 0.5 - x_0(\omega)$ ($\lambda > 0$).

As shown in Fig. 9(b), the relative center location approaches 0.5 with increasing N_S , confirming the asymmetry of non-Bloch response. The convergence of $x_{0,L}(\omega)$ and $x_{0,R}(\omega)$ further exhibits left-right excitation symmetry.

Data availability

The datasets generated during and/or analyzed during the current study are available from the corresponding author, Zhesen Yang, upon request.

Code availability

Code examples of key conclusions developed for this study and the software used are available in the GitHub repository at <https://github.com/oaddao/CFD-code-examples> and have been archived in Zenodo with the <https://doi.org/10.5281/zenodo.17404523>. Other codes are available from the authors upon request.

Received: 19 August 2025; Accepted: 22 January 2026;
Published online: 03 February 2026

References

- Ashida, Y., Gong, Z. & Ueda, M. Non-hermitian physics. *Adv. Phys.* **69**, 249–435 (2020).
- Bergholtz, E. J., Budich, J. C. & Kunst, F. K. Exceptional topology of non-hermitian systems. *Rev. Mod. Phys.* **93**, 015005 (2021).
- Zhang, X., Zhang, T., Lu, M.-H. & Chen, Y.-F. A review on non-hermitian skin effect. *Adv. Phys. X* **7**, 2109431 (2022).
- Lin, R., Tai, T., Li, L. & Lee, C. H. Topological non-hermitian skin effect. *Front. Phys.* **18**, 53605 (2023).
- Yao, S. & Wang, Z. Edge states and topological invariants of non-hermitian systems. *Phys. Rev. Lett.* **121**, 086803 (2018).
- Song, F., Yao, S. & Wang, Z. Non-hermitian topological invariants in real space. *Phys. Rev. Lett.* **123**, 246801 (2019).
- Kunst, F. K., Edvardsson, E., Budich, J. C. & Bergholtz, E. J. Biorthogonal bulk-boundary correspondence in non-hermitian systems. *Phys. Rev. Lett.* **121**, 026808 (2018).
- Lee, C. H. & Thomale, R. Anatomy of skin modes and topology in non-Hermitian systems. *Phys. Rev. B* **99**, 201103 (2019).
- Kawabata, K., Shiozaki, K., Ueda, M. & Sato, M. Symmetry and topology in non-hermitian physics. *Phys. Rev. X* **9**, 041015 (2019).
- Okuma, N., Kawabata, K., Shiozaki, K. & Sato, M. Topological origin of non-hermitian skin effects. *Phys. Rev. Lett.* **124**, 086801 (2020).
- Borgnia, D. S., Kruchkov, A. J. & Slager, R.-J. Non-hermitian boundary modes and topology. *Phys. Rev. Lett.* **124**, 056802 (2020).
- Zhang, K., Yang, Z. & Fang, C. Correspondence between winding numbers and skin modes in non-Hermitian systems. *Phys. Rev. Lett.* **125**, 126402 (2020).
- Yi, Y. & Yang, Z. Non-hermitian skin modes induced by on-site dissipations and chiral tunneling effect. *Phys. Rev. Lett.* **125**, 186802 (2020).
- Zhang, L. et al. Acoustic non-hermitian skin effect from twisted winding topology. *Nat. Commun.* **12**, 6297 (2021).
- Gu, Z. et al. Transient non-hermitian skin effect. *Nat. Commun.* **13**, 7668 (2022).
- Zhang, X., Tian, Y., Jiang, J.-H., Lu, M.-H. & Chen, Y.-F. Observation of higher-order non-Hermitian skin effect. *Nat. Commun.* **12**, 5377 (2021).
- Zhou, Q. et al. Observation of geometry-dependent skin effect in non-Hermitian phononic crystals with exceptional points. *Nat. Commun.* **14**, 4569 (2023).
- Weidemann, S. et al. Topological funneling of light. *Science* **368**, 311–314 (2020).
- Xiao, L. et al. Non-hermitian bulk-boundary correspondence in quantum dynamics. *Nat. Phys.* **16**, 761 (2020).

20. Lin, Q. et al. Observation of non-Hermitian topological Anderson insulator in quantum dynamics. *Nat. Commun.* **13**, 3229 (2022).
21. Liu, G.-G. et al. Localization of chiral edge states by the non-hermitian skin effect. *Phys. Rev. Lett.* **132**, 113802 (2024).
22. Lin, Q. et al. Topological phase transitions and mobility edges in non-hermitian quasicrystals. *Phys. Rev. Lett.* **129**, 113601 (2022).
23. Ghatak, A., Brandenbourger, M., Wezel, J. & Coulais, C. Observation of non-hermitian topology and its bulk-edge correspondence in an active mechanical metamaterial. *Proc. Natl. Acad. Sci. U.S.A.* **117**, 29561–29568 (2020).
24. Brandenbourger, M., Locsin, X., Lerner, E. & Coulais, C. Non-reciprocal robotic metamaterials. *Nat. Commun.* **10**, 1–8 (2019).
25. Chen, Y., Li, X., Scheibner, C., Vitelli, V. & Huang, G. Realization of active metamaterials with odd micropolar elasticity. *Nat. Commun.* **12**, 5935 (2021).
26. Wang, W., Wang, X. & Ma, G. Non-hermitian morphing of topological modes. *Nature* **608**, 50–55 (2022).
27. Helbig, T. et al. Generalized bulk-boundary correspondence in non-hermitian topoelectrical circuits. *Nat. Phys.* **16**, 747 (2020).
28. Hofmann, T. et al. Reciprocal skin effect and its realization in a topoelectrical circuit. *Phys. Rev. Res.* **2**, 023265 (2020).
29. Liu, S. et al. Non-hermitian skin effect in a non-hermitian electrical circuit. *Research* **2021**, 5608038 (2021).
30. Zou, D. et al. Observation of hybrid higher-order skin-topological effect in non-hermitian topoelectrical circuits. *Nat. Commun.* **12**, 7201 (2021).
31. Zhang, H., Chen, T., Li, L., Lee, C. H. & Zhang, X. Electrical circuit realization of topological switching for the non-hermitian skin effect. *Phys. Rev. B* **107**, 085426 (2023).
32. Kozii, V. & Fu, L. Non-hermitian topological theory of finite-lifetime quasiparticles: prediction of bulk fermi arc due to exceptional point. *Phys. Rev. B* **109**, 235139 (2024).
33. Nagai, Y., Qi, Y., Isobe, H., Kozii, V. & Fu, L. Dmft reveals the non-hermitian topology and fermi arcs in heavy-fermion systems. *Phys. Rev. Lett.* **125**, 227204 (2020).
34. Kaneshiro, S., Yoshida, T. & Peters, R. z_2 non-hermitian skin effect in equilibrium heavy-fermion systems. *Phys. Rev. B* **107**, 195149 (2023).
35. Geng, H. et al. Nonreciprocal charge and spin transport induced by non-Hermitian skin effect in mesoscopic heterojunctions. *Phys. Rev. B* **107**, 035306 (2023).
36. Shao, K. et al. Non-hermitian moiré valley filter. *Phys. Rev. Lett.* **132**, 156301 (2024).
37. Zhou, H. et al. Observation of bulk Fermi arc and polarization half charge from paired exceptional points. *Science* **359**, 1009–1012 (2018).
38. Shen, H. & Fu, L. Quantum oscillation from in-gap states and a non-Hermitian Landau level problem. *Phys. Rev. Lett.* **121**, 026403 (2018).
39. Yoshida, T., Peters, R., Kawakami, N. & Hatsugai, Y. Symmetry-protected exceptional rings in two-dimensional correlated systems with chiral symmetry. *Phys. Rev. B* **99**, 121101 (2019).
40. Rausch, R., Peters, R. & Yoshida, T. Exceptional points in the one-dimensional Hubbard model. *New J. Phys.* **23**, 013011 (2021).
41. Peters, R. & Yoshida, T. Hinge non-hermitian skin effect in the single-particle properties of a strongly correlated f -electron system. *Phys. Rev. B* **110**, 125114 (2024).
42. Bergholtz, E. J. & Budich, J. C. Non-Hermitian Weyl physics in topological insulator ferromagnet junctions. *Phys. Rev. Res.* **1**, 012003 (2019).
43. San-Jose, P., Cayao, J., Prada, E. & Aguado, R. Majorana bound states from exceptional points in non-topological superconductors. *Sci. Rep.* **6**, 21427 (2016).
44. Philip, T. M., Hirsbrunner, M. R. & Gilbert, M. J. Loss of hall conductivity quantization in a non-Hermitian quantum anomalous Hall insulator. *Phys. Rev. B* **98**, 155430 (2018).
45. Guan, F. et al. Overcoming losses in superlenses with synthetic waves of complex frequency. *Science* **381**, 766–771 (2023).
46. Guan, F. et al. Compensating losses in polariton propagation with synthesized complex frequency excitation. *Nat. Mater.* **23**, 506–511 (2024).
47. Zeng, K. & Zhang, S. Complex frequency analysis of coupled plasmonic systems (invited). *Acta. Optica. Sinica.* **44**, 1026019 (2024).
48. Li, H., Mekawy, A., Krasnok, A. & Alù, A. Virtual parity-time symmetry. *Phys. Rev. Lett.* **124**, 193901 (2020).
49. Archambault, A., Besbes, M. & Greffet, J.-J. Superlens in the time domain. *Phys. Rev. Lett.* **109**, 097405 (2012).
50. Tsakmakidis, K. L., Pickering, T. W., Hamm, J. M., Page, A. F. & Hess, O. Completely stopped and dispersionless light in plasmonic waveguides. *Phys. Rev. Lett.* **112**, 167401 (2014).
51. Tetikol, H. & Aksun, M. Enhancement of resolution and propagation length by sources with temporal decay in plasmonic devices. *Plasmonics* **15**, 2137–2146 (2020).
52. Tsakmakidis, K. & Wartak, M. *Metamaterials and Nanophotonics: Principles, Techniques and Applications* (World Scientific, 2022).
53. Kim, S., Lepeshov, S., Krasnok, A. & Alù, A. Beyond bounds on light scattering with complex frequency excitations. *Phys. Rev. Lett.* **129**, 203601 (2022).
54. Kim, S., Peng, Y.-G., Yves, S. & Alù, A. Loss compensation and superresolution in metamaterials with excitations at complex frequencies. *Phys. Rev. X* **13**, 041024 (2023).
55. Jiang, T. et al. Observation of non-hermitian boundary-induced hybrid skin-topological effect excited by synthetic complex frequencies. *Nat. Commun.* **15** (2024).
56. Huang, J., Ding, K., Hu, J. & Yang, Z. Complex frequency fingerprint: basic concept and theory. Preprint at: <https://doi.org/10.48550/arXiv.2411.12577> (2025).
57. Xue, W.-T., Li, M.-R., Hu, Y.-M., Song, F. & Wang, Z. Simple formulas of directional amplification from non-bloch band theory. *Phys. Rev. B* **103**, L241408 (2021).
58. Hu, Y.-M. & Wang, Z. Green's functions of multiband non-hermitian systems. *Phys. Rev. Res.* **5**, 043073 (2023).
59. Yokomizo, K. & Murakami, S. Non-bloch band theory of non-Hermitian systems. *Phys. Rev. Lett.* **123**, 066404 (2019).
60. Yang, Z., Zhang, K., Fang, C. & Hu, J. Non-hermitian bulk-boundary correspondence and auxiliary generalized Brillouin zone theory. *Phys. Rev. Lett.* **125**, 226402 (2020).
61. Haus, H. & Huang, W. Coupled-mode theory. *Proc. IEEE.* **79**, 1505–1518 (1991).
62. Huang, W.-P. Coupled-mode theory for optical waveguides: an overview. *J. Opt. Soc. Am. A* **11**, 963–983 (1994).
63. Li, Q., Wang, T., Su, Y., Yan, M. & Qiu, M. Coupled mode theory analysis of mode-splitting in coupled cavity system. *Opt. Express* **18**, 8367–8382 (2010).
64. Fan, S., Suh, W. & Joannopoulos, J. D. Temporal coupled-mode theory for the Fano resonance in optical resonators. *J. Opt. Soc. Am. A* **20**, 569–572 (2003).
65. Suh, W., Wang, Z. & Fan, S. Temporal coupled-mode theory and the presence of non-orthogonal modes in lossless multimode cavities. *IEEE J. Quantum Electron.* **40**, 1511–1518 (2004).

Acknowledgements

J. Huang and Z.Y. were sponsored by the National Key R&D Program of China (No. 2023YFA1407500), China Postdoctoral Science Foundation (No. 2025M773351) and the National Natural Science Foundation of China (No. 12322405, 12104450, 12047503). J. Hu was sponsored by the Ministry of Science and Technology (Grant No. 2022YFA1403901), National Natural Science Foundation of China (No. 12494594), and the New Cornerstone Investigator Program.

Author contributions

Z. Yang conceived and supervised the research and acquired funding. J. Huang led the computational work, conducted the theoretical analysis and derivations, created the visualizations, and drafted the original manuscript. J. Hu contributed to the validation of the results through active discussion and data interpretation and acquired research funding. Both J. Hu and Z. Yang were involved in revising and editing the manuscript.

Competing interests

The authors declare no competing interests.

Additional information

Supplementary information The online version contains supplementary material available at <https://doi.org/10.1038/s42005-026-02524-8>.

Correspondence and requests for materials should be addressed to Jiangping Hu or Zhesen Yang.

Peer review information *Communications Physics* thanks the anonymous reviewers for their contribution to the peer review of this work.

Reprints and permissions information is available at <http://www.nature.com/reprints>

Publisher's note Springer Nature remains neutral with regard to jurisdictional claims in published maps and institutional affiliations.

Open Access This article is licensed under a Creative Commons Attribution-NonCommercial-NoDerivatives 4.0 International License, which permits any non-commercial use, sharing, distribution and reproduction in any medium or format, as long as you give appropriate credit to the original author(s) and the source, provide a link to the Creative Commons licence, and indicate if you modified the licensed material. You do not have permission under this licence to share adapted material derived from this article or parts of it. The images or other third party material in this article are included in the article's Creative Commons licence, unless indicated otherwise in a credit line to the material. If material is not included in the article's Creative Commons licence and your intended use is not permitted by statutory regulation or exceeds the permitted use, you will need to obtain permission directly from the copyright holder. To view a copy of this licence, visit <http://creativecommons.org/licenses/by-nc-nd/4.0/>.

© The Author(s) 2026